Three-Dimensional Model for Sand Structures on the Continental Shelf, Part II: The Interaction of Internal Waves and the Bottom Topography

Juan Mario Restrepo
Mathematics and Computer Science Division
Argonne National Laboratory, Argonne IL U.S.A. 60439

Jerry L. Bona
Mathematics Department
The Pennsylvania State University, University Park PA U.S.A. 16802

Preprint MCS-P407-1293,
Mathematics and Computer Science Division
Argonne National Laboratory, Argonne, IL, 1993

Abstract

Longshore sand ridges are frequently observed to occur on the continental shelf where the overlying ocean is stratified. This study formulates a model for the formation and evolution of three-dimensional longshore sand ridges on the continental shelf. The model is based on the interaction of interfacial, weakly nonlinear waves in a stratified ocean with the sedimentary bottom topography.

1 Introduction

Longshore sand ridges are underwater barlike features composed of loose granular sediment. Sand ridges hundreds of meters long and up to a few meters high are usually found in groups, arranged in more or less parallel rows separated from each other by hundreds of meters oriented normal or at some small angle to the direction in which the overlying water waves propagate [McBride & Moslow1991].

Shallow-water, weakly nonlinear interfacial waves appear as highly coherent groups having well-defined wavelength and are observed propagating shoreward on a density stratification, such as the picnocline. Their crests are generally oriented along isobaths [Apel1979, Baines1981]. Their wavelengths range from 200 to 1600 meters, depending on the depth, which can be considerably larger than the local water column depth. An estimate of the energy contained in the larger ones is in the order of 0.1 MJ/m^2. They have been seen to appear twice a day in some areas, coinciding with the tidal cycle, and originate mostly in places where there are sharp changes in the bottom topography, such as on the edge of the continental shelf. Since the contribution of coriolis forces in this problem is negligible (i.e., the wave periods for the waves under consideration range between fractions of a minute and an hour), the sole forcing agent is gravitational. As the density stratification collapses in the shallower reaches of the shelf, the water column is no longer able to support an internal wave. Hence, in our formulation of the model for the internal wave case, we assume that the wave field is strictly unidirectional.

As a result of experimental observations of sand structures acted upon by water waves [Boczar-Karakiewicz, Amos & Drapeau1990], a two-dimensional model for the formation and evolution of sand ridges was proposed in [Boczar-Karakiewicz, Bona & Cohen1986]. This model was informally tested against field data, and based on encouraging results, was extended to three-dimensions, with the aim of making it more relevant to the ocean setting [Restrepo & Bona1993]. In addition to complementing this last study, the present study shows how the mechanism may be extended to the situation in which a simply stratified ocean approximation is needed. The primary motivation for considering the stratified case is that the mechanism is applicable in the deeper reaches of the continental shelf, and for reasons given later, it may be easier to test in the ocean setting than the version presented in [Restrepo & Bona1993]. A secondary motivation is to show how this model accounts for time-dependent forcing.

Referring to Figure 1, we envision infragravity waves coming into the purview of the model at the line $x = 0$, where the long waves begin "feeling" the bottom topography. The shoreward direction, x, increases as the wave travels shoreward. The spanwise direction, given by y, is approximately parallel to the line of constant phase of the incoming waves. The waves propagate shoreward, possibly at an angle with respect to the prevailing direction of maximum gradient of the bottom topography. The extent of the model is limited in the longshore direction by the disintegration of the interface supporting the internal waves, by the approach to the breaking zone, by any singularity in the depth, or by significant energy transfer from low to high frequencies, reflecting a severe imbalance between nonlinear and

dispersive effects in the wave train. The spanwise direction is limited by the same sort of issues. The absence of a reflected component originating, perhaps, in the shoaling region may be justified by the collapse of the density stratification in the shallower reaches of the shelf, the water column no longer being able to support an internal wave.

Field data from the continental shelf suggests that there are two time scales: a fast time scale t, which measures the evolution of the fluid quantities, and a long time scale T which measures the evolution of the bottom topography. In addition, the data suggests that the typical height and slope of the longshore sand ridges, represented in this study by the function h, is such that $\varepsilon = O(\nabla^n h) = O(\alpha)$, where α is a small-valued parameter typical of the ratio of the amplitude of the water waves to the depth of the water column below the fluid interface in an assumed two-density fluid. Furthermore, the type of longshore sand ridge under consideration is such that longshore spatial variation is larger than the spatial variations of the fluid quantities. It is proposed that the sand ridge shoreward variation be $X = \alpha x$. Hence, two scales of shoreward variation exist, so that

$$\partial_x \rightarrow \partial_x + \alpha \partial_X \tag{1}$$

$$\partial_t \rightarrow \partial_t + \alpha \partial_\tau. \tag{2}$$

We will assume in this study that the conditions are such that $\partial_\tau = 0$. The bottom in scaled variables may be represented by

$$h(X, y, T) = 1 + \varepsilon f(X, y, T), \tag{3}$$

where the function $f = O(1)$.

The plan of this paper is as follows. In Section 2, the main hydrodynamical issues for the internal waves are considered, as well as the mass transport problem. In order to illustrate the main features of the model, Section 3 presents a few computed examples, followed in Section 4 with some closing remarks and suggestions for future work.

2 The Hydrodynamics

We begin by developing the Hamiltonian formulation to the two-fluid internal wave problem, relying on Bowman's work [Bowman1986]. As illustrated in Figure 2, the domain is described by $\Omega_1 \approx \mathbf{R}^2 \times [-H, \eta]$, and $\Omega_2 = \mathbf{R}^2 \times [\eta, D]$. The lower layer (1) has a uniform density ρ_1, and the upper layer (2) a density $\rho_2 < \rho_1$. The fluid is subjected solely to gravitational forcing. The velocity field is now given in each layer by $(\mathbf{u}, w)_i$, where the subscript refers to layer 1 or 2. The interface between the two fluids is given by $z = \eta(\mathbf{r}, t)$ and the bottom by $z = -H(\mathbf{r}, T)$. The transverse variable $\mathbf{r} = (x, y)$, where x increases shoreward and y is the spanwise coordinate. The fluid is assumed incompressible and irrotational in each layer. In terms of a scalar potential, the velocity is given by $(\mathbf{u}, w)_i = \nabla_3 \phi_i$. From conservation of mass, the equations of motion within the fluid are $\Delta_3 \phi_i = 0$, in Ω_i. At the interface, the pressure is continuous; hence the dynamical boundary condition is $\phi_{i,t} = -\frac{1}{2} |\nabla_3 \phi_i|^2 - g\rho_i \eta$, at $z = \eta$.

The bottom, which is assumed impermeable, has a normal velocity that agrees with that of the fluid. Thus $\phi_{1,z} = -\nabla H \cdot \nabla \phi_1$ at $z = -H$. The kinematic condition on the interface is $\frac{D(z-\eta)}{Dt} = 0$, or $\phi_{i,z} = \eta_t + \nabla \phi_i \cdot \nabla \eta$ at $z = \eta$. Finally, we make the simplifying "rigid-lid" assumption

$$\phi_{2,z} = 0, \text{ at } z = D, \tag{4}$$

the constant air-water interface.

With conjugate variables η and $\mathbf{U} \equiv \rho_2 \nabla \phi_2 - \rho_1 \nabla \phi_1$ the Hamiltonian system that yields the description of the dynamics of the internal waves takes the form

$$\begin{aligned} \eta_t &= -\nabla \cdot (\frac{\delta E}{\delta \mathbf{U}}) \\ \mathbf{U}_t &= -\nabla (\frac{\delta E}{\delta \eta}), \end{aligned} \tag{5}$$

where the Hamiltonian E is numerically equal to the sum of the potential and the kinetic energy for this problem.

The potential energy is simply

$$V = \int_{\mathbf{R}^2} d^2 r \frac{1}{2} g(\rho_1 - \rho_2)\eta^2. \tag{6}$$

The total kinetic energy is the sum of contributions from both layers; thus

$$K = \rho_1 \int_{\mathbf{R}^2} d^2 r \int_{-H}^{\eta} \frac{1}{2} |\nabla_3 \phi_1|^2 dz + \rho_2 \int_{\mathbf{R}^2} d^2 r \int_{-\eta}^{D} \frac{1}{2} |\nabla_3 \phi_2|^2 dz = K_1 + K_2. \tag{7}$$

Define the parameters $\alpha \ll 1$, and $\beta \ll 1$. Assume that $O(\alpha) \sim O(\beta^2)$, and take $H = O(1)$, $\nabla H = O(\alpha)$, $\eta = O(\alpha)$, $\Phi = O(\alpha)$. Further, consider the differentiations $\partial_z, \partial_t, \nabla = O(\beta)$.

Referring to the results from [Restrepo & Bona1993], we calculate the kinetic energy in the lower layer using an approximation for the velocity potential,

$$\begin{array}{ccccccc} \phi_1(\mathbf{r}, z, t) = & \Phi_1(\mathbf{r}, t) & - & \frac{1}{2} z^2 \nabla^2 \Phi_1(\mathbf{r}, t) & - & z \nabla \cdot (H \nabla \Phi_1(\mathbf{r}, t)), \\ & O(\alpha) & & O(\alpha\beta^2) & & O(\alpha\beta^2) \end{array}$$

so that

$$K_1 = \rho_1 \int_{\mathbf{R}^2} d^2 r \{\frac{1}{2}(H + \eta)(\nabla \Phi_1)^2 + \frac{H}{2}(\nabla H \cdot \nabla \Phi_1)^2 - \frac{H^3}{6}(\nabla^2 \Phi_1)^2\}, \tag{8}$$

which is an expression of $O(\alpha^3 \beta^2)$ and $O(\alpha^2 \beta^4)$.

The boundary condition given by Equation (4) can be exploited to find K_2 as a surface integral. Using Green's theorem and assuming that the gradients of the potential tend to zero as $|\mathbf{r}| \to \infty$, we have

$$K_2 = -\rho_2 \int_{\mathbf{R}^2} d^2 r \nabla \Phi_1 \nabla \Phi_2. \tag{9}$$

Define the pseudo-differential operator $G \equiv -k\coth(HkD)$. Its precise structure is a result of satisfying the boundary conditions on the interface and on the ocean surface. Adding the expressions for K_1 and K_2, using the definition of $\mathbf{U}$, and the operator G, we obtain as the total kinetic energy

$$K = \frac{1}{2}\int_{\mathbf{R}^2} d^2r\{\frac{1}{\rho_1}(H+\eta)\mathbf{U}^2 + \frac{H^2\rho_2}{\rho_1^2}\mathbf{U}\cdot G\mathbf{U} + \frac{\rho_2 H}{\rho_1^2}(\nabla H\cdot\mathbf{U})^2\} + O(\alpha^3\beta^2), \tag{10}$$

or rearranging,

$$K = \frac{1}{2}\int_{\mathbf{R}^2} d^2r\{\frac{1}{\rho_1}[(H+\eta) - \frac{H^2\rho_2}{\rho_1^2 D}]\mathbf{U}^2 + \frac{H^2\rho_2}{\rho_1^2}\mathbf{U}\cdot M\mathbf{U} + \frac{\rho_2 H}{\rho_1^2}(\nabla H\cdot\mathbf{U})^2\} + O(\alpha^3\beta^2), \tag{11}$$

where $M = \frac{I}{D} + G = \frac{1}{D} - k\coth(HkD)$.
Depending on the size of D/λ, there are three physically distinct possibilities:

- If $D/\lambda \ll 1$, then $\mathbf{U}\cdot M\mathbf{U} = O(\alpha^2 D/\lambda^2)$, and $M \approx 1/D - \frac{D\nabla^2}{3}$. For this case, the terms $\eta\mathbf{U}\cdot\mathbf{U}$ and $\mathbf{U}\cdot M\mathbf{U}$ balance if $\alpha^2 D/\lambda^2 \sim 1$. A Boussinesq system is obtained.
- If $D/\lambda \sim 1$, then $\mathbf{U}\cdot M\mathbf{U} = O(\alpha^2/\lambda)$. For this case, if $\alpha\lambda^2/D \sim 1$, the result is the intermediate long-wave equation.
- If $D/\lambda \gg 1$, then $\mathbf{U}\cdot M\mathbf{U} = O(\alpha^2/\lambda)$, and $M \approx |k|$. If $\alpha\lambda \sim 1$, the outcome is the Benjamin-Ono equation.

Note that this last case corresponds to a very deep upper layer, lying over a thinner lower layer, and hence is not considered relevant in this study. In the ocean setting the density stratification is most appropriately described by a continuous function with respect to depth. However, if a two-fluid approximation is adequate, the relevant case to the problem at hand among those presented above is the first one.

By substituting the expressions for the potential and kinetic energy, Equations (6) and (11), into Equation (5), the general equation for the dynamics of the internal wave field is obtained:

$$\begin{aligned} \eta_t &= -\nabla\cdot\{[\tfrac{1}{\rho_1}(H+\eta) - \tfrac{H^2\rho_2}{\rho_1^2 D}]\mathbf{U}\} - \tfrac{\rho_2}{\rho_1^2}\nabla\cdot\{H(\nabla H)^2\mathbf{U} + H^2 M\mathbf{U}\} \\ \mathbf{U}_t &= -\nabla\cdot\{\tfrac{1}{2\rho_1^2}\mathbf{U}\cdot\mathbf{U} + (\rho_1-\rho_2)g\eta\}. \end{aligned} \tag{12}$$

The result from linear theory may be recovered by neglecting second- and higher-order terms in Equation (12). The solutions proportional to $\exp\{i(kx-\omega t)\}$ satisfy

$$\begin{aligned} \omega\eta &= (\tfrac{1}{\rho_1} - \tfrac{\rho_2 H}{\rho_1^2 D} + \tfrac{\rho_2 HM}{\rho_1^2})kHU \\ \omega U &= k(\rho_1-\rho_2)g\eta. \end{aligned} \tag{13}$$

Thus,

$$c^2 \equiv \frac{\omega^2}{k^2} = \frac{g(\rho_1 - \rho_2)}{\rho_1}[1 - \frac{\rho_2}{\rho_1} Hk \coth(kD)]. \tag{14}$$

The relevant case in this study is the first one:

$$\begin{aligned} \eta_t &= -\nabla\cdot\{\tfrac{1}{\rho_1}(H+\eta)\mathbf{U}\} - \tfrac{\rho_2}{\rho_1^2}\nabla\cdot\{H(\nabla H)^2\mathbf{U} + \tfrac{1}{3}H^2 D\nabla\nabla\cdot\mathbf{U}\} \\ \mathbf{U}_t &= -\nabla\cdot\{\tfrac{1}{2\rho_1^2}\mathbf{U}\cdot\mathbf{U} + (\rho_1 - \rho_2)g\eta\}. \end{aligned} \tag{15}$$

Equation (12) may be shown to be linearly unstable [Bona1975]. To circumvent this problem, we carry out an ad-hoc procedure that "regularizes" the equation. The lowest-order relations

$$\begin{aligned} \eta_t &= -\nabla\cdot\{\tfrac{1}{\rho_1}H\mathbf{U}\} \\ \mathbf{U}_t &= -\nabla\{(\rho_1 - \rho_2)g\eta\} \end{aligned} \tag{16}$$

are used to modify the troublesome parts of the dispersive terms to get the regularized model for the hydrodynamics relevant in this study, namely,

$$\begin{aligned} \eta_t &= -\nabla\cdot\{\tfrac{1}{\rho_1}(H+\eta)\mathbf{U}\} + \tfrac{D\rho_2}{3\rho_1^2}\nabla\cdot[\nabla(H\eta_t)] \\ \mathbf{U}_t &= -\nabla\{\tfrac{1}{2\rho_1^2}\mathbf{U}\cdot\mathbf{U} + (\rho_1 - \rho_2)g\eta\}. \end{aligned} \tag{17}$$

Let $\gamma \equiv \frac{(\rho_1 - \rho_2)}{\rho_1}$ be the Boussinesq parameter, and let the typical thickness of the lower layer be h_0. The scaling adopted here is

$$t \leftarrow \frac{\sqrt{gh_0}\,t}{\lambda} \quad \mathbf{U} \leftarrow \frac{\sqrt{h_0}\mathbf{U}}{\rho_1\sqrt{g}a} \quad \eta \leftarrow \eta/a \quad h \leftarrow \frac{H}{h_0} \quad d \leftarrow \frac{D}{h_0} \quad \mathbf{r} \leftarrow \frac{\mathbf{r}}{\lambda}, \tag{18}$$

where the convention $new \leftarrow scale \times old$ is being used. Equation (17) is, in scaled variables,

$$\begin{aligned} \eta_t + \nabla\cdot\{\tfrac{1}{\rho_1}(h+\alpha\eta)\mathbf{U}\} - d\beta^2\tfrac{\rho_2}{3\rho_1}\nabla\cdot[\nabla(h\eta_t)] &= 0 \\ \mathbf{U}_t + \nabla\{\tfrac{1}{2}\mathbf{U}\cdot\mathbf{U} + \gamma\eta\} &= 0. \end{aligned} \tag{19}$$

Additionally, the spanwise variables are scaled to reflect the weak spanwise dependence of the waves:

$$y \leftarrow \xi^{1/2}y \qquad \hat{y}\cdot\mathbf{u} \leftarrow \xi^{-1/2}\hat{y}\cdot\mathbf{u}. \tag{20}$$

We think of $\xi = O(\alpha^{1/2})$.

The substitution of a uniform expansion of the form

$$\begin{aligned} \eta &= f_0 + \alpha^1 f_1 + \alpha^2 f_2 + \cdots \\ \mathbf{U} &= \mathbf{g}_0 + \alpha^1\mathbf{g}_1 + \alpha^2\mathbf{g}_2 + \cdots \end{aligned} \tag{21}$$

into Equation (19), followed by matching order by order yields the internal wave equation to lowest orders in α.

Explicitly, after crossdifferentiating Equation (19),

$$\begin{array}{lll} \alpha^0: & \mathcal{L}\eta_0 & = 0 \\ \alpha^1: & \mathcal{L}\eta_1 & = \mathcal{G}_1(\eta_0, u_0, v_0, G; x, X, y, t) \\ \alpha^2: & \mathcal{L}\eta_2 & = \mathcal{G}_2(\eta_0, u_0, v_0, \eta_1, u_1, v_1, G; x, X, y, t) \end{array} \tag{22}$$

where

$$\begin{array}{lll} \mathcal{L} & = & \partial_{tt} - \gamma\partial_{xx} - d\frac{\beta^2\rho_2\partial_{xxtt}}{3\rho_1}, \\ G & = & \frac{\varepsilon}{\alpha} f(X, y, T). \end{array} \tag{23}$$

The inhomogeneous term in the first-order equation is given by

$$\begin{array}{lll} \mathcal{G}_1 & = & (\gamma + d\frac{\beta^2\rho_2\partial_{tt}}{3\rho_1})\eta_{0yy} + G(\gamma + d\frac{2\beta^2\rho_2\partial_{tt}}{3\rho_1})\eta_{0xx} + 2(\gamma + d\frac{\beta^2\rho_2\partial_{tt}}{3\rho_1})\eta_{0xX} \\ & & +(u_0^2/2)_x - (u_0\eta_0)_{xt}. \end{array} \tag{24}$$

Assuming that lowest-order wave packet expansion for the surface velocity is of the form

$$u_0(x, X, y, t) \;=\; \textstyle\sum_{j=1}^{3} a_j(X, y)e^{i(k_j x - \omega_j t)} + c.c.., \tag{25}$$

and making use of the lowest-order relation $u_{0t} + \gamma\nabla\eta_0 = 0$ to obtain the surface amplitude

$$\eta_0(x, X, y, t) = \sum_{j=1}^{3} \frac{\omega_j}{\gamma k_j} a_j(X, y)e^{i(k_j x - \omega_j t)} + c.c. \tag{26}$$

we are able to obtain a lowest order description of the internal waves in terms of wave packets centered at k_j with support $\Delta k_j < k_j$. A solution of the above-mentioned form is possible if the relation between the frequency and wavenumber of the wave carriers satisfies the dispersion relation, having inconsistently assumed that the dispersive term operates at all orders,

$$\omega_j^2 - \frac{k_j^2}{\gamma + d\beta^2\frac{\rho_2 k_j^2}{3\rho_1}} = 0. \tag{27}$$

The solution must also satisfy the compatibility condition

$$\frac{jk_1}{2\pi}\int_{X_0}^{X_0+2\pi/jk_1} e^{\pm ijk_1 x}(\mathcal{G}_j + \mathcal{G}_j^\star)dx = 0, \text{where } j = 1, 2, 3, \tag{28}$$

starred quantities conjugated.

As discussed in [Restrepo & Bona1993], only weak resonance is to be expected. Substituting Equations (25) and (26) into Equation (22) and applying the compatibility condition, we obtain, for the weakly resonant triad case in which $k_2 = 2k_1 - \delta$, $\omega_2 = 2\omega_1$, where the detuning parameter $\delta \leq 0$, the equations for spatial variation of the first two wave packets:

$$\begin{array}{rcl} a_{1x} + i\varepsilon f D_1 E_1 a_1 - i\xi F_1 a_{1yy} + i\alpha D_1 S_1 e^{-i\delta x} a_1^\star a_2 & = & 0 \\ a_{2x} + i\varepsilon f D_2 E_2 a_2 - i\xi F_2 a_{2yy} + i\alpha D_2 S_2 e^{+i\delta x} a_1^2 & = & 0, \end{array} \tag{29}$$

to $O(\delta/X)$. The constants are

$$\begin{aligned} D_j &= 1/2(1 - d\frac{\rho_2\beta^2\omega_j^2}{3\rho_1}) \\ E_j &= k_j(\gamma - d\frac{2\rho_2\beta^2\omega_j^2}{3\rho_1} \\ F_j &= 1/2k_j \\ S_1 &= \frac{k_2-k_1}{\omega_1}\{k_2 - k_1 + \frac{\omega_1}{\gamma}(\frac{\omega_1}{k_1} + \frac{\omega_2}{k_2})\} \\ S_2 &= \frac{2}{\omega_2}k_1^2 + 2\omega_1^2. \end{aligned} \tag{30}$$

For three wave packet weak resonance the relation among the frequency and wavenumbers $\omega_j = j\omega_1$, $k_2 = 2k_1 - \delta$, and $k_3 = 3k_1 - \Delta$ is given by the dispersion relation. The procedure is the same as the two wave group case and yields

$$\begin{aligned} a_{1x} + i\varepsilon f D_1 E_1 a_1 - i\xi F_1 a_{1yy} + i\alpha D_1 S_{211} e^{-i\delta_x} a_1^\star a_2 + i\alpha D_1 S_{321} e^{i\Delta_x} a_2^\star a_3 &= 0 \\ a_{2x} + i\varepsilon f D_2 E_2 a_2 - i\xi F_2 a_{2yy} + i\alpha D_2 S_2 e^{+i\delta_x} a_1^2 + i\alpha D_2 S_{312} e^{i\Delta_x} a_1^\star a_3 &= 0 \\ a_{3x} + i\varepsilon f D_3 E_3 a_3 - i\xi F_3 a_{3yy} + i\alpha D_3 S_3 e^{-i\Delta_x} a_1 a_2 &= 0, \end{aligned} \tag{31}$$

to $O(\delta/X)$. The constants are, with subscripts $1, 2$, or 3,

$$\begin{aligned} D_j &= 1/2(1 - \frac{d\rho_2\beta^2\omega_j^2}{3\rho_1}) \\ E_j &= k_j(\gamma - \frac{2d\rho_2\beta^2\omega_j^2}{3\rho_1}) \\ F_j &= 1/2k_j \\ S_3 &= \frac{k_2+k_1}{\omega_3}\{k_2 + k_1 + \frac{3\omega_1}{\gamma}(\frac{\omega_1}{k_1} + \frac{\omega_2}{k_2})\} \\ S_2 &= \frac{2}{\omega_2}k_1^2 + 2\omega_1^2 \\ S_{ijl} &= \frac{k_i-k_l}{l\omega_1}\{k_i - k_j + \frac{l\omega_1}{\gamma}(\frac{\omega_i}{k_i} + \frac{\omega_j}{k_j})\}. \end{aligned} \tag{32}$$

In this study we restrict our attention to the triad case.

2.1 The Mass Transport Problem

The drift velocity is the second-order steady state flow in the sediment-laden boundary layer that hugs the bottom topography generated by the passage of the overlying water waves. The boundary layer is assumed to have a characteristic thickness $\delta_{bl} \ll h_0$. For simplicity the sediment in the boundary layer is assumed to move from place to place at a rate equal to the drift velocity.

In order to compute the drift velocity, an explicit expression for the fluid velocity immediately outside of the sediment-laden boundary layer is required. From inviscid theory, in scaled variables, the shoreward velocity is explicitly

$$\begin{aligned} U_b &\equiv \gamma\hat{x}\cdot\mathbf{U}(\mathbf{r}, -h, t) \\ &= \gamma u(\mathbf{r}, t) - \gamma\beta^2\{-h[(hu_{xx}(\mathbf{r}, t)) + \xi(hv_{xy}(\mathbf{r}, t))] + \tfrac{1}{2}h^2(u_{xx}(\mathbf{r}, t) + \xi v_{xy}(\mathbf{r}, t))\}, \end{aligned} \tag{33}$$

and the span-wise velocity

$$\begin{aligned} V_b &\equiv \gamma\hat{y}\cdot\mathbf{U}(\mathbf{r},-h,t) \\ &= \gamma v(\mathbf{r},t) - \gamma\beta^2\{-h[(hu_{xy}(\mathbf{r},t)) + \xi(hv_{yy}(\mathbf{r},t))] + \tfrac{1}{2}h^2(u_{xy}(\mathbf{r},t) + \xi v_{yy}(\mathbf{r},t))\} \end{aligned} \tag{34}$$

in the neighborhood of the boundary layer. The bottom velocities to lowest order are

$$\begin{aligned} U_{0b} &= \gamma(u_0 + \beta^2\tfrac{h^2}{2}u_{0xx}) \\ &= \textstyle\sum_{j=1}^2 C_j a_j(X,y)e^{i(k_jx-\omega_jt)} + c.c. \\ V_{0b} &= \gamma v_0 + \gamma\beta^2\tfrac{(h^2)_y}{2}u_{0x} + \gamma\beta^2\tfrac{h^2}{2}u_{0xy} \\ &= -i\textstyle\sum_{j=1}^2 \tfrac{1}{k_j}[C_j a_{jy}(X,y) + i\gamma\beta^2\tfrac{k_j}{2}(h^2)_y]e^{i(k_jx-\omega_jt)} + c.c., \end{aligned} \tag{35}$$

where $C_j = \gamma(1-\beta^2k_j^2\frac{h^2}{2})$.

As shown in [Restrepo & Bona1993], for high Reynolds flows, the equations of motion in the boundary layer are given by

$$\begin{aligned} \beta\tilde{u}_{0t} - \tilde{u}_{0nn} &= \beta U_{0bt} \\ \beta\tilde{v}_{0t} - \tilde{v}_{0nn} &= \beta V_{0bt} \\ p_{0n} &= 0 \\ \beta\tilde{u}_{0x} + \tilde{w}_{0n} &= 0, \end{aligned} \tag{36}$$

to lowest order.

A solution of Equation (36) of the form

$$\tilde{u}_l = \sum_{j=1}^{2}\alpha^l P_l(x,y,n)e^{i(k_jx-\omega_jt)} + c.c., \tag{37}$$

with a similar representation for $\tilde{v}_l$, subject to no-slip boundary conditions on the bottom and matching of the inviscid solution to the boundary layer solution sufficiently far above from the bottom, is found by integrating Equation (36). The result is

$$\begin{aligned} \tilde{u}_0 &= \textstyle\sum_{j=1}^2 C_j a_j(1-e^{-n\Lambda_j})e^{i(k_jx-\omega_jt)} + c.c. \\ \tilde{v}_0 &= i\textstyle\sum_{j=1}^2 k_j(\beta^2(h^2)_y a_j/2 - C_j a_{jy}/k_j^2)(1-e^{-n\Lambda_j})e^{i(k_jx-\omega_jt)} + c.c. \\ \tilde{w}_0 &= i\beta\textstyle\sum_{j=1}^2 k_jC_ja_j(1-n\Lambda_j - e^{-n\Lambda_j})/\Lambda_j e^{i(k_jx-\omega_jt)} + c.c., \end{aligned} \tag{38}$$

where $\Lambda_j = (1-i)\sqrt{\beta\omega_j/2}$. The vertical velocity $\tilde{w}$ is found by integrating the continuity equation.

The drift velocity [Longuett-Higgins1953] is given by

$$\begin{aligned} \mathcal{U} &= \langle u_1\rangle + \langle\textstyle\int^t \tilde{u}_0 d\tilde{t}\tilde{u}_{0x}\rangle + \langle\textstyle\int^t \tilde{w}_0 d\tilde{t}\tilde{u}_{0n}\rangle \\ \mathcal{V} &= \langle v_1\rangle + \langle\textstyle\int^t \tilde{u}_0 d\tilde{t}\tilde{v}_{0x}\rangle + \langle\textstyle\int^t \tilde{w}_0 d\tilde{t}\tilde{v}_{0n}\rangle. \end{aligned} \tag{39}$$

It is assumed that the viscous boundary layer is sediment-laden, composed of cohesionless, rarely interacting sand particles.

The mass transport equation [Restrepo & Bona1993] is

$$\frac{\partial h(x,y,T)}{\partial T} = \frac{K}{\rho_0}(\mu_x + \nu_y), \tag{40}$$

where ρ_0 is the mean sediment concentration and μ and ν are the shoreward mass flux and the longshore mass flux, respectively:

$$\begin{aligned} \mu &\equiv \int_0^{\delta_{bl}} \rho(x,z')\mathcal{U}(x,z'))dz' \\ \nu &\equiv \int_0^{\delta_{bl}} \rho(x,z')\mathcal{V}(x,z'))dz'. \end{aligned} \tag{41}$$

Note that when weak y dependence scaling is adopted in Equation (40) the longshore mass flux is $O(\xi^2)$ smaller than the shoreward flux.

In the remainder of this study, we assume, for simplicity, that the sediment concentration is constant and equal to ρ_0 in the boundary layer. In terms of Equation (39), and upon use of Equation (41), the mass flux components, to lowest order, are

$$\mu = \sum_{j=1}^{2} \frac{2k_j C_j^2 |a_j|^2}{\omega_j \sigma_j} \mathcal{I}_{1j} + \sum_{j=1}^{2} \frac{\beta k_j C_j^2 |a_j|^2}{\sigma_j^3} \mathcal{I}_{2j} + c.c., \tag{42}$$

where

$$\begin{aligned} \mathcal{I}_{1j} &= \sigma_j \delta_{bl} - \frac{\beta\sigma_j}{2} - \frac{3}{2} + \frac{1}{2}(1-\beta\sigma_j)e^{-2\sigma_j\delta_{bl}} \\ &\quad + e^{-\sigma_j\delta_{bl}}[\cos\sigma_j\delta_{bl} - \sin\sigma_j\delta_{bl}][1-\beta\sigma_j(\sigma_j\delta_{bl}+1)] \end{aligned} \tag{43}$$

and

$$\begin{aligned} \mathcal{I}_{2j} &= \frac{3}{2}(1/2 - \sigma_j\delta_{bl}) + e^{-2\sigma_j\delta_{bl}}/4 \\ &\quad - e^{-\sigma_j\delta_{bl}}[1+\delta_{bl}\sigma_j]\cos\sigma_j\delta_{bl} + 2e^{-\sigma_j\delta_{bl}}\sin\sigma_j \end{aligned} \tag{44}$$

for the shoreward mass flux, and

$$\nu = \sum_{j=1}^{2} \frac{iC_j^2 a_j^\star a_{jy}}{\omega_j \sigma_j} \mathcal{J}_j + O(\beta^3) + c.c. \tag{45}$$

for the longshore directed mass flux, with

$$\begin{aligned} \mathcal{J}_j &= \sigma_j\delta_{bl} - 1 - \frac{1}{2}(1-e^{-2\sigma_j\delta_{bl}}) + e^{-\sigma_j\delta_{bl}}(\cos\sigma_j\delta_{bl} - \sin\sigma_j\delta_{bl}) \\ &\quad + \beta\Lambda_j[\frac{1}{2}(1+e^{-2\sigma_j\delta_{bl}}) + e^{-\Lambda_j\delta_{bl}}(i\delta_{bl}\sigma_j/2 - 1)]. \end{aligned} \tag{46}$$

The quantities $\mathcal{I}_{11}$, $\mathcal{I}_{21}$, and $\mathcal{J}_1$ are plotted parametrically in Figures 3, 4, and 5.

The hydrodynamic forcing, which shows up in the boundary conditions $a_i(x = 0, y)$, may be changing in time. Since the adjustment time for the water waves is in time scales greater than t, it is suggested that the boundary conditions that appropriately reflect variable forcing condition is $a_i(0, y) = \mathcal{A}_i(y, T)$. To summarize, then, the internal waves are obtained by solving the system

$$\begin{aligned} a_{1x} - iK_1 a_{1yy} + iK_3 f(x,y) a_1 + iK_5 e^{-i\delta_x} a_1^\star a_2 &= 0 \\ a_{2x} - iK_2 a_{2yy} + iK_4 f(x,y) a_2 + iK_6 e^{+i\delta_x} a_1^2 &= 0 \\ a_1(x=0,y) &= \mathcal{A}_1(y,T) \\ a_2(x=0,y) &= \mathcal{A}_2(y,T) \end{aligned} \tag{47}$$

plus appropriate boundary conditions on $y = 0$ and $y = N$. The K coefficients are $O(\alpha, \varepsilon)$, and are given by Equation (29) and Equation (30). The bottom evolution, on the other hand, is Equation (40):

$$\begin{aligned} \frac{\partial}{\partial T} h(x,y,T) &= \frac{K}{\rho_0}(\mu_x + \nu_y) \\ h(x,y,0) &= \mathcal{H}(x,y). \end{aligned} \tag{48}$$

Equations (47) and (48) constitute the full model.

The solution of the system is achieved by using the following prescription: The initial bottom configuration $\mathcal{H}(x, y)$ determines the function $f(x, y)$ in Equation (47) at $T = 0$. The flow on the interface is found by solving Equation (47). The drift velocities μ and ν are computed and used in Equation (48) to update the bottom h. The new bottom is then used in the triad equations, and the whole process is repeated until some T final. In the iteration process the boundary conditions are updated, should the conditions for the forcing are time dependent.

3 Qualitative Features of the Solutions

Some of the main qualitative features of the full model were presented in [Restrepo & Bona1993]. Further examples are presented here and are meant to give the reader a more complete picture of the model's behavior.

To better discern the effects of different bottom topographies on the internal waves and on the eventual bottom topography after the passage of many waves, we now turn to the case in which the initial bottom configurations are strictly x-dependent and the boundary conditions are constant. Briefly, in this case, a larger number of bars form when the gradient is slight, the distance separating the bars increases seaward for the positively sloped case, and initial bottom discontinuities in the x direction tend get "smoothed out" after the passage of many waves.

Figure 6 shows the bottom topography, which was

$$f(x,y,0) = \begin{cases} 0.005x & x > 180.0 \\ 0 & \text{otherwise} \end{cases} \tag{49}$$

at $T = 0$. The lighter line represents the bottom profile at $T = 20\Delta T$; the darker line is the bottom at $T = 80\Delta T$. The parameters are $\alpha = 0.1$, $\varepsilon = 0.2$, $\beta = 0.36$, and $\omega_1 = 1.2$. For the same range of parameters, Figure 7 shows the effect on the surface and on the eventual bottom of an initial topography that is approximately tuned to the interaction length of the surface waves.

A bottom that initially had gradients in the y direction bends the water waves, affecting the eventual bottom topography by producing a series of bars with refractive features. Consider, for example, the case in which the initial bottom topography is $f(x, y) = 0.0075x - 0.005y$, the domain is $240\Delta x$ in length, and all other parameters as before. Figure 8 shows the refracting bottom at $T = 400\Delta T$. A striking way in which refraction takes place can be seen in the case for which the boundary conditions at $x = 0$ are y dependent. Shown in Figure 9 for $f(T = 400\Delta T)$ is the case for which $f(x, y) = 0$ at $T = 0$ and the boundary conditions are $\mathcal{A}_1 = 0.5 + 0.001y$ and $\mathcal{A}_2 = 0.02 + 0.001y$, corresponding to an incoming gravity wave that has slightly higher amplitude at one end than at the other.

Interesting configurations are achieved when the above-mentioned effects are combined. Figure 10 illustrates the refraction pattern on one of the packet centers for which $\mathcal{A}_1 = 0.5 - 0.001y$, $\mathcal{A}_2 = 0.1 - 0.001y$, and the bottom at $T = 0$ was $f(x, y) = 0.01y$.

Another curious change in pattern direction is illustrated in Figure 11. In this case $\mathcal{A}_1 = 0.5 - 0.001y$, $\mathcal{A}_2 = 0.1 + 0.001y$, and the bottom at $T = 0$ is $f(x, y) = 0.01y$. All the parameters in Figure 11 are the same as those in Figure 10.

4 Concluding Discussion

This study shows how internal waves on the continental shelf, supported by the interface in a two-fluid idealization of the stratified ocean, may be capable of generating structures on a sandy bottom that resemble sand ridges. It is conjectured that a significant but by no means exclusive agent for the formation and evolution of sand ridges is the second-order boundary layer drift velocity that results from the passage of overlying nonlinear dispersive waves with wavelengths that are significantly greater in extent than the local water column depth. Since the scouring action of the drift velocity has wave-like spatial structure, it produces coherent undulating patterns on the sandy bottom. While there are several types of sand ridges (and most likely, a variety of sources for their formation), our model represents (albeit crudely) a sensible explanation for the formation of longshore sand ridges that occur on the continental shelf, far from the shoaling area, in which wave breaking is a rare occurrence, the wave field is nearly devoid of a reflected component, and a simply stratified water column is present.

While linear nondispersive gravity waves can produce a second-order drift velocity in the boundary layer hugging the bottom topography, we conjecture that weakly nonlinear dispersive water waves are more likely to be the agents of formation. The claim is that there exists a closer correlation between interbar spacing and the interaction length rather than with the wavelength of the waves, which would be the case for linear waves. The interaction length is a local quantity which coincides with the distance in which the most energetic interactions in the spectrum of the nonlinear water waves takes place, rather than the recurrence distance

which some authors have supposed [Elgar, Freilich & Guza1991]. In the two wave packet case this distance would correspond to the length in which energetic interactions between the wave packets takes place and happens to coincide with the recurrence as defined [Elgar, Freilich & Guza1991] for the two-mode case.

Preliminary experimental evidence supports the claim that a relation may exist between the features of the nonlinear long waves and the bars. Boczar-Karakiewicz et al. [Boczar-Karakiewicz, Paplinska & Winieki1981], in a series of laboratory experiments, observed a relationship between the frequency, the amplitude, and the dispersion, in the waves and the bar spacing. As described in our model, the interaction length is a nonlinear relation that depends on the frequency, the dispersion, and the nonlinearity of the wave. For the two-dimensional case with a flat bottom the dependence of the interaction length as a function of the detuning parameter is portrayed in Figure 12. Figure 13 and Figure 14 illustrate the dependence of the interaction length on the size of the nonlinear parameter α, and the dispersion parameter β. The relevant size of the parameters α and β in the sand ridge case is as high as 0.15 for α, and $0.005 < \beta < 0.15$. From the graphs it may be inferred that the interaction length is more sensitive to dispersion than to nonlinearity for the above-mentioned ranges of α and β in qualitative agreement with the aforementioned experiments.

An interesting question that has thus far received little attention is the subject of steady-state bottom configurations. In numerical simulations of the present model it has been observed that a common but by no means exclusive long-time outcome for the evolution of the bottom topography is one in which the structure of the wave packet centers and that of the bottom have similar qualitative features. It is also quite common in these numerical simulations for the bottom to reach its steady state in a gradual fashion rather than in small spurts of high activity followed by relative inactivity, a common observation in the formation of sand ripples [Boczar-Karakiewicz, Benjamin & Pritchard1987]. Since the temporal characterization of the evolution of actual sand ridges has not yet been systematically measured, it is difficult at present to judge whether the temporal behavior of the sand ridges created with the present model is in fact correct.

A number of interesting aspects of sand ridge dynamics require field observations. One is the measurement and characterization of the boundary layer velocities and the search for observational evidence of a periodic structure in the drift velocity that can be correlated in some way to the passing waves. Another interesting observational project is the measurement of the evolution of the spectra of internal waves in sand ridge evolution time scales, the aim being to discern how the waves change with morphological changes in the bottom topography. By far the most difficult experiment would entail the observation of the actual evolution of the bottom topography. If the working assumption is that there may be a variety of agents contributing to the formation and maintenance of sand ridges, we need to thoroughly understand the present model and/or improve upon it with an eye towards developing a clearly verifiable experimental criteria that will enable us to differentiate this mechanism from any other, since a naive comparison between the present model and field data will contribute little to the validation of the conjectured mechanism. Since interfacial internal waves of the sort relevant to the conjecture are, in some instances, more readily identifiable in

the ocean setting than are the surface waves; since they usually develop as strictly progressive waves; and since the place at which they originate, say, a large promontory or the edge of the continental shelf, and the location where the stratification is no longer significant, can be fixed in the ocean setting, the model presented in this study could conceivably be tested with some confidence, we hope to generate interest among observational oceanographers so that such experiments may be carried out. Some comparisons have been carried out with available data from the coast of Eastern Australia and New Foundland, however, the data was incomplete.

Beardsley et al. [Beardsley et al.1985] have shown that in areas off the coast of Eastern United States the stratification required to support the propagation of internal waves occurs only during summer, a period in which less sedimentary movement has been observed. While there is data that shows that there is a noticeable increase of motion of sandy material during winter storms, the authors do not imply that no sediment movement occurs at other times of the year over seasonal time scales. Furthermore, the appearance of winter storms does not explain the high degree of order in the ridges. The conclusion that sand ridges cannot be formed by internal nonlinear long waves which may pack energy in the order of hundreds of thousands of watts-minute would be correct if it was proven that storms were the only agent for flows strong enough to produce sand movement. The truth is probably that there are many agents for the formation of sand ridges, among them, we believe could be the mechanism presented in this study.

It is not that surprising that little is known about sand ridges in the deeper reaches of the continental shelf from direct field measurements. While more field data is being collected and analyzed, our best recourse at present is to keep pursuing the development of models such as the one presented here. An increased understanding of its inner workings may yield clues to the dynamics of this beautiful natural phenomenon.

5 Acknowledgments

We thank the Applied Research Laboratory at The Pennsylvania State University for making this project possible. This work was also supported by the Office of Scientific Computing, U.S. Department of Energy, under Contract W-31-109-Eng-38.

6 References

[Apel1979] Apel, J. R., "Observations of Internal Wave Signatures in ASTP Photographs," in *Apollo-Soyuz Test Project. Summary Science Report* #SP-H12, NASA, 1979, 505–509.

[Baines1981] Baines, P. G., "Satellite Observations of Internal Waves on the Australian North-West Shelf," *Australian Journal of Marine and Freshwater Research* 32 (1981), 457–463.

dsley et al.1985] Beardsley, R. C., D. C. Chapman, K. H. Brink, S. R. Ramp & R. Schlitz, "The Nantucket Shoals Flux Experiment. Part I: A Basic Despcription of the Current and Temperature Variability," *Journal of Physical Oceanography* 15 (1985), 713–748.

& Drapeau1990] Boczar-Karakiewicz, B., C. L. Amos & G. Drapeau, "The Origin and Stability of Sand Ridges on Sable Island Bank, Scotian Shelf," *Continental Shelf Research* 10 (1990), 683–701.

Pritchard1987] Boczar-Karakiewicz, B., T. B. Benjamin & W. P. Pritchard, "Reflection of Water Waves in a Channel with Corrugated Bed," *Journal of Fluid Mechanics* 185 (1987), 229–247.

a & Cohen1986] Boczar-Karakiewicz, B., J. L. Bona & G. Cohen, *Interaction of Shallow-water waves and bottom topography*, PSU Applied Mathematics Series #AM3, Penn State University, 1986.

& Winieki1981] Boczar-Karakiewicz, B., B. Paplinska & J. Winieki, "Formation of Sandbars by Surface Waves in Shallow Water. Laboratory Experiments," *Rozprawy Hydrotechnisczne* (1981).

[Bona1975] Bona, J. L., "On the stability theory of solitary waves," *Proc. Roy. Soc. London Ser. A* 344 (1975), 363–374.

[Bowman1986] Bowman, S., "Hamiltonian Formulations and Long-Wave Models for Two-Fluid Systems," unpublished, 1986.

ch & Guza1991] Elgar, S., M. Freilich & R. T. Guza, "Recurrence in Truncated Boussinesq Models of Nonlinear Waves in Shallow Water," *Journal of Geophysical Research* 95 (1991), 11547–11556.

ett-Higgins1953] Longuett-Higgins, M. S., "Mass Transport in Water Waves," *Philosophical Transactions of the Royal Society of London* 245 (1953), 535–581.

& Moslow1991] McBride, R. A. & T. F. Moslow, "Origin, Evolution, and Distribution of Sand Ridges, Atlantic Inner Shelf, U.S.A.," *Marine Geology* 97 (1991), 57–85.

po & Bona1993] Restrepo, J. M. & J. L. Bona, "Model for the Formation of Longshore Sand Ridges on the Continental Shelf," Mathematics and Computer Science Division, Argonne, Ill, December 1993.

List of Figures

1 Aerial view of the problem 16
2 Side view, internal wave problem 16
3 Variation of $\mathcal{I}_{11}$, with $\delta_{bl} = 1.0$ fixed 17
4 Variation of $\mathcal{I}_{21}$, with $\delta_{bl} = 1.0$ fixed 17
5 Parametric plot of $\mathcal{J}_1$, with $\delta_{bl} = 1.0$ fixed 17
6 Cross-section of $f(x, y, T)$. The bottom was initially sloped but featureless. The darker line represents the bottom at $T = 80\Delta T$, whereas the lighter line represents the bottom at $T = 20\Delta T$. 18
7 Effect of a tuned bottom, $f = 0.5\sin(0.412x)$ at $T = 0$, on the eventual topography and ocean surface: Light solid line. Bottom at $T = 100\Delta T$: Dark solid line. 18
8 Refraction due to initial bottom configuration. Bottom at $T = 100\Delta T$. Shown here is the difference between the new bottom and the original topography. . 19
9 Refraction due to boundary conditions. Bottom at $T = 100\Delta T$. 19
10 Refraction due to antagonistic boundary conditions and initial bottom configuration. a_2 at $T = 0$. 20
11 Refraction due to boundary conditions and initial bottom configuration. a_1 at $T = 0$. 20
12 Interaction length dependence on the nonlinear parameter δ. The detuning parameter is scaled so that as $\delta \to 0$, $m \to 1$. 21
13 Interaction length dependence on the nonlinear parameter α. 21
14 Interaction length dependence on the dispersion parameter β. 21

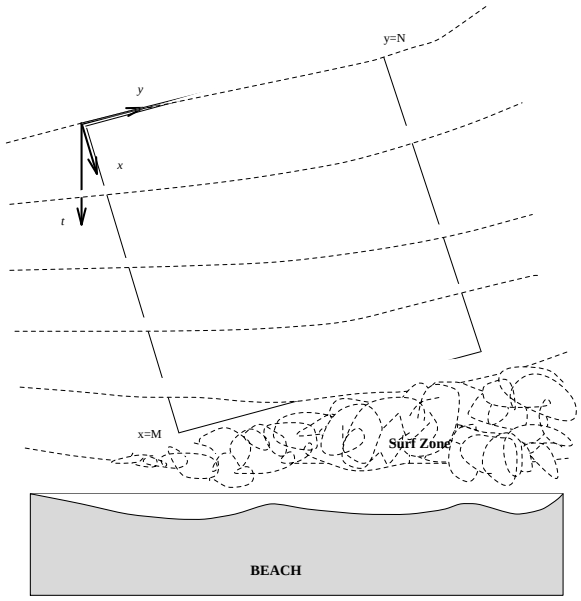

Figure 1: Aerial view of the problem

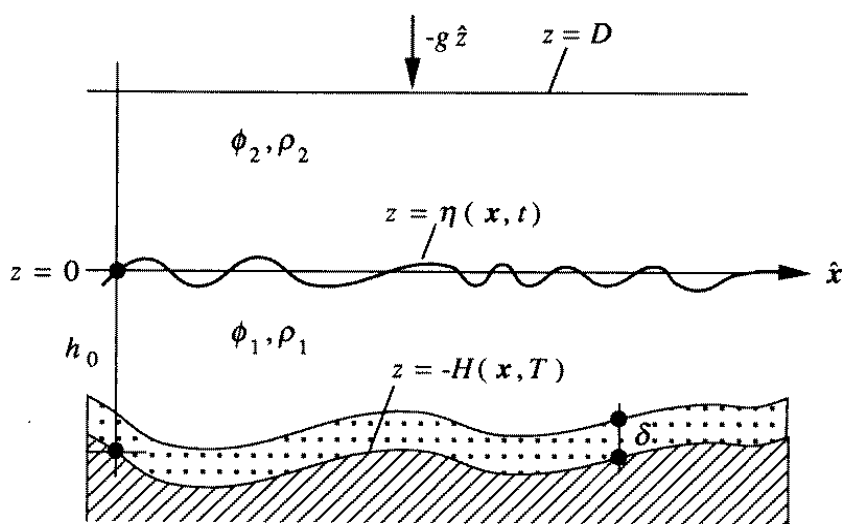

Figure 2: Side view, internal wave problem

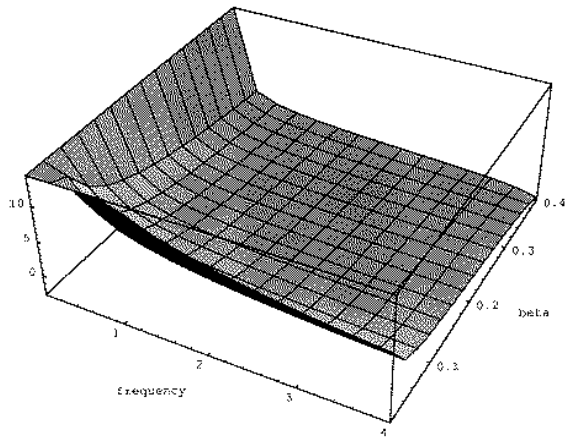

Figure 3: Variation of $\mathcal{I}_{11}$, with $\delta_{bl} = 1.0$ fixed

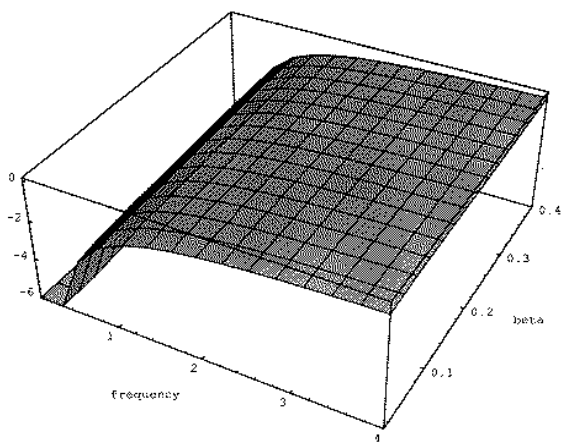

Figure 4: Variation of $\mathcal{I}_{21}$, with $\delta_{bl} = 1.0$ fixed

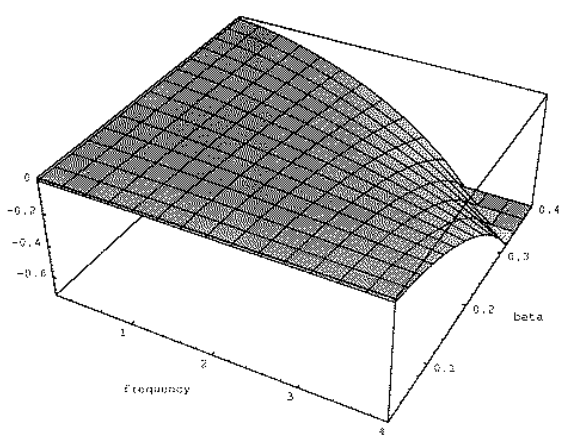

Figure 5: Parametric plot of $\mathcal{J}_1$, with $\delta_{bl} = 1.0$ fixed

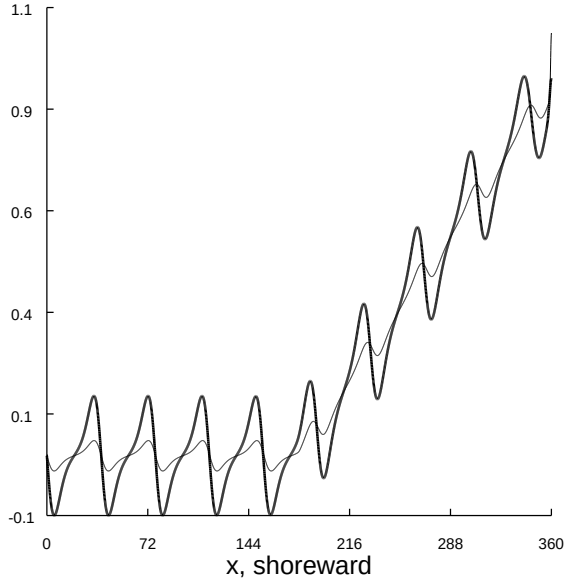

Figure 6: Cross-section of $f(x, y, T)$. The bottom was initially sloped but featureless. The darker line represents the bottom at $T = 80\Delta T$, whereas the lighter line represents the bottom at $T = 20\Delta T$.

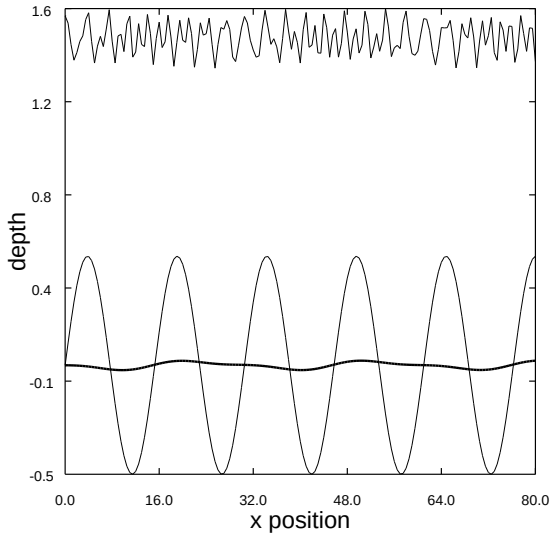

Figure 7: Effect of a tuned bottom, $f = 0.5\sin(0.412x)$ at $T = 0$, on the eventual topography and ocean surface: Light solid line. Bottom at $T = 100\Delta T$: Dark solid line.

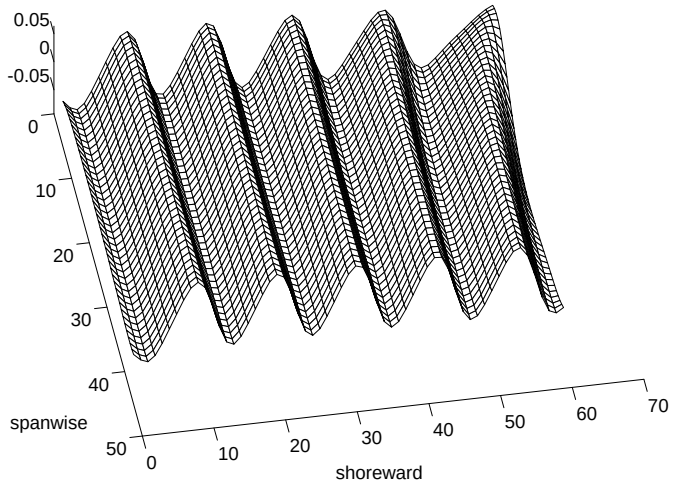

Figure 8: Refraction due to initial bottom configuration. Bottom at $T = 100\Delta T$. Shown here is the difference between the new bottom and the original topography.

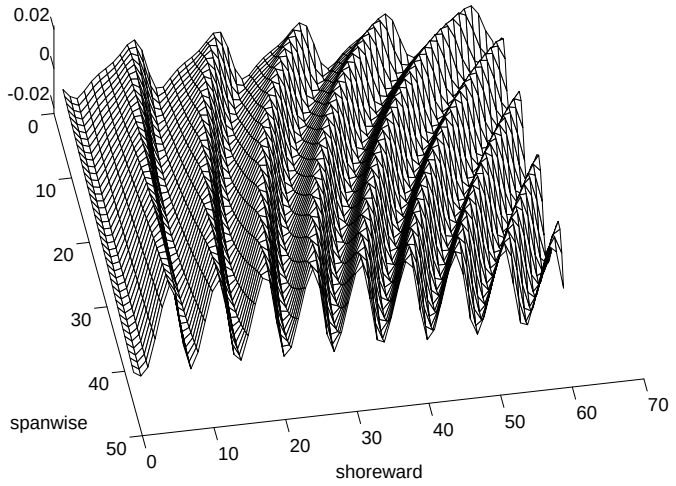

Figure 9: Refraction due to boundary conditions. Bottom at $T = 100\Delta T$.

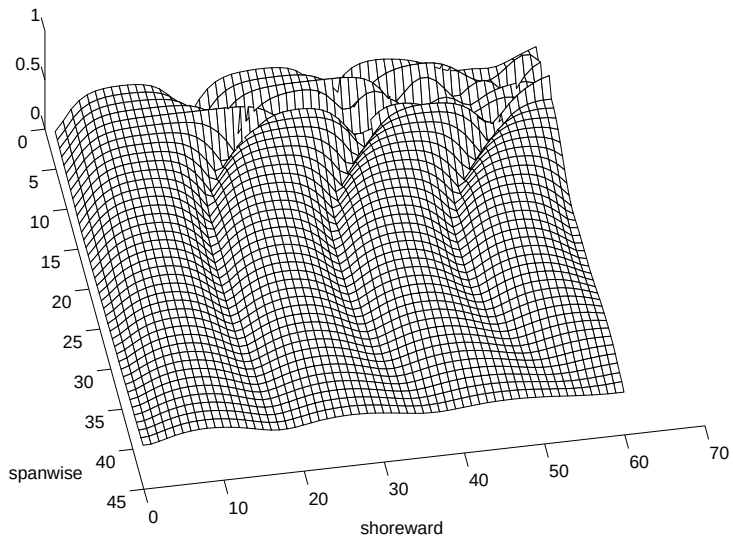

Figure 10: Refraction due to antagonistic boundary conditions and initial bottom configuration. a_2 at $T = 0$.

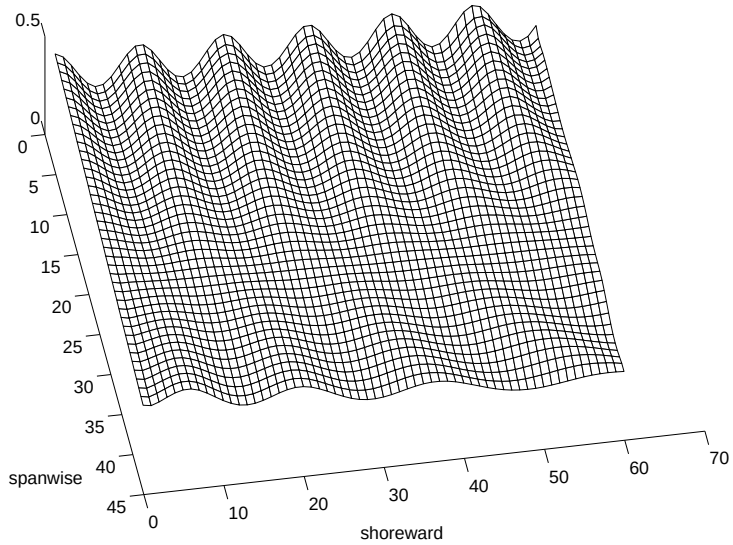

Figure 11: Refraction due to boundary conditions and initial bottom configuration. a_1 at $T = 0$.

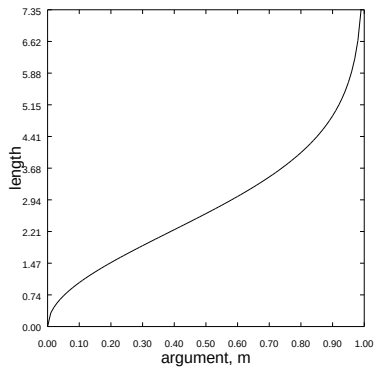

Figure 12: Interaction length dependence on the nonlinear parameter δ. The detuning parameter is scaled so that as $\delta \to 0$, $m \to 1$.

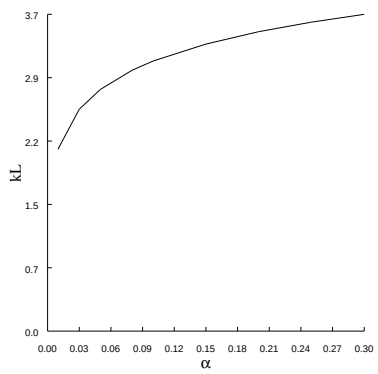

Figure 13: Interaction length dependence on the nonlinear parameter α.

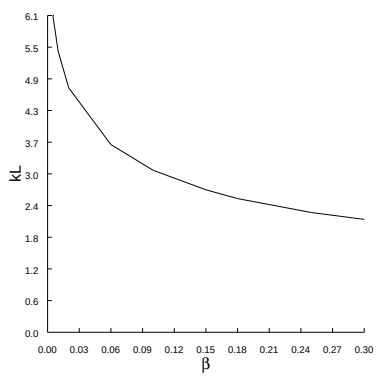

Figure 14: Interaction length dependence on the dispersion parameter β.